Mon. Not. R. Astron. Soc. **000**, 1–11 (2001) Printed 27 February 2001 (MN LATEX style file v1.4)

The Munich Near-Infrared Cluster Survey – I. Field selection, object extraction, and photometry

N. Drory,[1⋆†] G. Feulner,[1⋆] R. Bender,[1⋆] C. S. Botzler,[1] U. Hopp,[1⋆] C. Maraston,[1] C. Mendes de Oliveira,[2⋆] J. Snigula[1⋆]

[1] *Universitäts-Sternwarte München, Scheinerstr. 1, D-81679 München, Germany*
[2] *Instituto Astronômico e Geofísico, Av Miguel Stéfano 4200, 04301-904, São Paulo, Brazil*

Accepted –; Received –;

ABSTRACT

The Munich Near-IR Cluster Survey (MUNICS) is a wide-area, medium-deep, photometric survey selected in the K' band. It covers an area of roughly one square degree in the K' and J near-IR pass-bands. The survey area consists of $16\ 6' \times 6'$ fields targeted at QSOs with redshifts $0.5 < z < 2$ and $7\ 28' \times 13'$ stripes targeted at 'random' high Galactic latitude fields. Ten of the QSO fields were additionally imaged in R and I, and $0.6\ \mathrm{deg}^2$ of the randomly selected fields were also imaged in the V, R, and I bands. The resulting object catalogues were strictly selected in K', having a limiting magnitude (50 per cent completeness) of $K' \sim 19.5$ mag and $J \sim 21$ mag, sufficiently deep to detect passively evolving systems up to a redshift of $z \lesssim 1.5$ and luminosity of $0.5L^*$. The optical data reach a depth of roughly $R \sim 23.5$ mag. The project's main scientific aims are the identification of galaxy clusters at redshifts around unity and the selection of a large sample of field early-type galaxies at $0 < z < 1.5$ for evolutionary studies. In this paper – the first in a series – we describe the survey's concept, the selection of the survey fields, the near-IR and optical imaging and data reduction, object extraction, and the construction of photometric catalogues. Finally, we show the $J-K'$ vs. K' colour–magnitude diagramme and the $R-J$ vs. $J-K'$, $V-I$ vs. $J-K'$, and $V-I$ vs. $V-R$ colour–colour diagrammes for MUNICS objects, together with stellar population-synthesis models for different star-formation histories, and conclude that the data set presented is suitable for extracting a catalogue of massive field galaxies in the redshift range $0.5 \lesssim z \lesssim 1.5$ for evolutionary studies and follow-up observations.

Key words: surveys – infrared: galaxies – galaxies: photometry – galaxies: evolution – cosmology: observations

1 INTRODUCTION

Directly observing the evolution of individual galaxies with time is, unfortunately, not possible. Therefore we must rely on investigating the statistical properties of the whole galaxy population as a function of redshift, trying to draw conclusions from ensemble properties on the evolution of typical members of these ensembles, and thus facing difficulties, like, for example, discriminating between luminosity evolution and number density evolution.

Much work has been invested in this field, resulting in a lot of progress in the last decade which has seen many imaging and redshift surveys being undertaken using different selection techniques in wave-bands from the UV to the sub-mm. These surveys have a wide range of scientific applications, from the detection of high-redshift galaxy clusters to the study of the evolution of 'normal' field galaxies.

The earlier optically and near-IR selected redshift and imaging surveys, among others **?**), **?**), **?**), **?**), and **?**), laid the path to the landmark CFRS (Canada-France Redshift Survey; **?**), an I-band selected redshift survey mapping the evolution of the galaxy population out to $z \sim 1$. Also many 'pencil-beam' surveys have been carried out, the most prominent being the Hubble Deep Field North and South (**?**; **?**) and their ground-based imaging and spectroscopic follow-ups, allowing us a first glimpse at the galaxy population at $2.5 \lesssim z \lesssim 4.5$. The inability to determine redshifts spectroscopically for all objects where multi-band imaging data is available (because of limited telescope resources, either in observing time or in collecting area), caused photometric redshift determination techniques to gain attention again (**?**; **?**; **?**; **?**). This, and the wide-field imagers becoming available in the optical and also in the near-

⋆ Visiting astronomer at the German-Spanish Astronomical Center, Calar Alto, operated by the Max-Planck-Institut für Astronomie, Heidelberg, jointly with the Spanish National Commission for Astronomy.

† Visiting astronomer at the McDonald Observatory, Ft. Davis, Texas, operated by the University of Texas at Austin.

infrared wavelength regime, made multi-band imaging surveys a very promising option for further studies in galaxy evolution.

Selection in in a single pass-band introduces different (and sometimes subtle) selection effects, a well-known fact which need not necessarily be considered at the disadvantage of the resulting object database, as long as the selection function is well-understood and under control. These selection effects can be used deliberately for probing different galaxy populations and different aspects of their evolution. While selection in blue pass-bands is used to study star forming sources, selection in the near-IR is predominantly sensitive to the light of old stellar populations. Near-IR k-corrections are small even at redshifts above unity and insensitive to the spectral type of the observed objects (**?**) and to short-lived bursts of star formation, as has been pointed out by **?**). Thus near-IR selected surveys are thought to be much less biased with respect to the mix of spectral types compared to optically selected surveys. Furthermore, the uncertainties resulting from inhomogeneous dust absorption are minimal in the near-IR. It has therefore been concluded that near-IR selection is a feasible attempt at a selection in stellar mass (**?**; **?**).

The Munich Near-Infrared Cluster Survey (MUNICS) is an attempt at closing the gap between previously undertaken infrared-selected deep pencil-beam surveys (**?**; **?**; **?**; **?**; **?**; **?**) and relatively shallow wide-area surveys (**?**; **?**; **?**), simultaneously profiting from the advantages of near-infrared selection.

MUNICS is a wide-area, medium-deep, photometric survey selected in the K' band. One part of the surveyed fields was centred on known quasars, while the rest was randomly selected at high Galactic latitudes. It covers an area of roughly one square degree in the K' and J bands with optical follow-up imaging in the I, R, and V bands for a large fraction of the total surveyed area.

The resulting object catalogues are strictly selected in K' with a limiting magnitude of $K' \sim 19.5$ mag and $J \sim 21$ mag, sufficiently deep to detect passively evolving systems up to a redshift of $z \lesssim 1.5$ and luminosity of $0.5L^*$ (see Fig. 1). The optical data reach a depth of roughly $R \sim 23.5$ mag.

This paper is laid out as follows. Section 2 deals with the survey's scientific aims and concept. The required sensitivity in terms of limiting magnitudes, the selection of the survey fields as well as the photometric system adopted are described. In Section 3 we give an overview of the observations and discuss the reduction of the near-IR and optical imaging data. Section 4 contains the data analysis. The methods for object detection, photometry, and object classification are discussed, and a first analysis of the survey's completeness as well as number counts in five colours are presented.

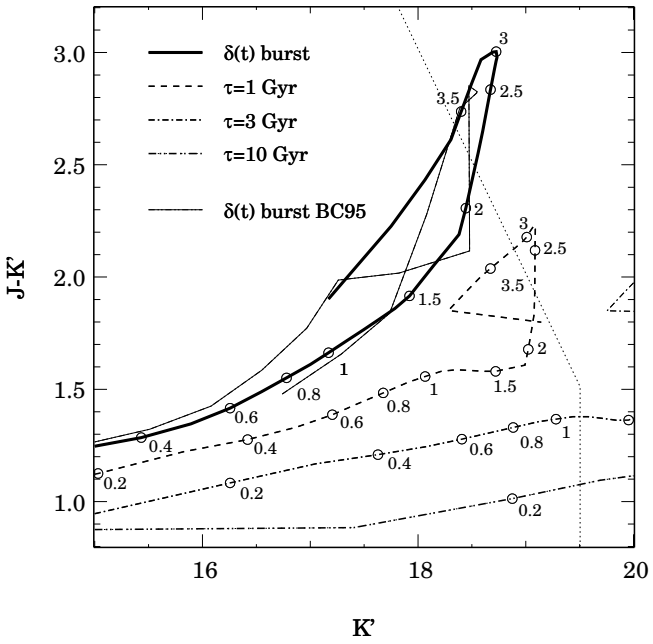

Figure 1. Stellar population synthesis models in the $J-K'$ vs. K' plane for different star-formation histories, a $\mathrm{SFR}(t) \propto \delta(t)$ burst at $z = 4$, and 3 exponential star formation rates $\mathrm{SFR}(t) \propto \exp(t/\tau)$ with $\tau = 1$, 3, and 10 Gyr, setting in at $z = 4$. The models are normalised to have a luminosity of L_B^* at the present epoch, according to the type-dependent luminosity function of the Virgo cluster (see text) as given by Sandage, Binggeli, & Tammann (1985). The thin dotted line indicates the limiting depth (50 per cent completeness) of the MUNICS data in J and K'. The adopted cosmology is $H_0 = 65, \Omega_0 = 0.3, \Omega_\Lambda = 0.7$. The SSP models used in the synthesis are from Maraston (1998). Additionally, an SSP model by Bruzual & Charlot (1995) is shown for comparison as a thin solid line.

2 SURVEY CONCEPT AND LAYOUT

2.1 Scientific aims

The project's main scientific aims are the following. First, to identify clusters of galaxies at high redshift by detecting their luminous early-type galaxy population. As has been shown in the last years, the early-type galaxy population in clusters is well in place at redshifts of at least 0.8 (**?**; **?**; **?**; **?**). Given the small k-corrections in the K band, this makes selection in the near-IR a promising approach to detect clusters at redshifts around unity, complementing selection in other optical bands. Clusters of galaxies allow to find large numbers of massive galaxies at higher redshift and thus represent unique laboratories to study the evolution of galaxies in high-density regions as a function of redshift, and in contrast to the evolution of similar galaxies in the field. Furthermore, the evolution of the number density of clusters is a promising test of cosmological models, depending sensitively on the density parameter Ω_0 (**?**; **?**; **?**; **?**). While the number of clusters known at redshifts $z > 0.5$ is steadily increasing (mostly due to X-ray selection), samples selected *uniformly* in the optical and near-IR wavelength ranges are still deficient.

Cluster detection at high redshifts is strongly biased towards the most massive systems, mainly because of lack of detection sensitivity for lower mass systems. Finding also less massive systems is important when reasoning about hierarchical galaxy formation models, since the galaxies in the densest environments formed earlier, so by looking only at the most dense environments one is effectively pushing the epoch of collapse, merging, and star formation out to higher redshifts and further away from the observational window. Therefore we decided to centre a subset of the MUNICS fields on known quasars hoping to increase the chance of detecting clusters in their environment.

Secondly, a statistically well-defined sample of the early-type galaxy population *in the field* can be constructed from our catalogues, which will be used to study the evolutionary history of such objects in the redshift range $0 < z < 1$ by means of the K-band selected luminosity function, the luminosity density at near-infrared wavelengths, and the two-point correlation function. Again, K-band selection offers unique opportunities due to the close connection between near-IR luminosity and stellar mass (**?**), and thus allows direct assessment of the predictions of hierarchical galaxy formation theories.

Thirdly, the nature of extremely red objects (EROs; **?**; **?**) will

be examined. EROs, usually defined in terms of $R-K$ greater than or approximately equal to 5 at moderately faint K-band magnitudes of $K \geq 18$, are thought to be either high-redshift early-type galaxies or heavily extincted starburst galaxies (**?**; **?**), the relative contribution of the two sub-populations being yet highly uncertain. Due to the small areas of the surveys available so far, even the surface density of these objects is not reliably known (**?**). Since they mostly are R-band 'dropouts', having the possibility to detect such objects in the MUNICS data in the I and J bands, together with the large field covered, will enable us to gain valuable information on their nature.

2.2 Limiting sensitivity

Fig. 1 shows stellar population synthesis models in the $J-K'$ vs. K' plane for different star-formation histories, a $\mathrm{SFR}(t) \propto \delta(t)$ Simple Stellar Population (SSP), and 3 exponential star formation rates $\mathrm{SFR}(t) \propto \exp(t/\tau)$ with $\tau = 1$, 3, and 10 Gyr. The onset of star formation occurs at $z = 4$ in all models. The populations are normalised to have a luminosity of L_B^* at the present epoch, according to the type-dependent luminosity function of the Virgo cluster as given by **?**). The adopted values for M_B^* are $M_B^* = -21.5$ for the SSP model (elliptical/S0 galaxy), $M_B^* = -20.5$ for $\tau = 1$ (Sa–Sb spiral), $M_B^* = -19.5$ for $\tau = 3$ (Sc), and $M_B^* = -17.5$ for $\tau = 10$ (Sd and later). The cosmology is $H_0 = 65\ \mathrm{km\,s^{-1}\,Mpc^{-1}}, \Omega_0 = 0.3, \Omega_\Lambda = 0.7$.

The SSP models are taken from **?**). The distinguishing feature of that synthesis method is the adaption of the fuel consumption theorem to evaluate the energetics of the post main-sequence evolutionary phases. The models used here have solar metallicity and age ranging from 30 Myr to 15 Gyr. The Initial Mass Function (IMF) is a power law $\Psi(M) \propto M^{-(1+x)}$ with Salpeter exponent $x = 1.35$ down to a lower mass limit of $0.1 M_\odot$. The optical and infrared colours predicted by these SSP models are calibrated against Milky Way and Magellanic Cloud globular clusters and compared to similar models from the literature in **?**). Fig. 1 also shows an SSP model by **?**) using the 1995 version of their code, with solar metallicity and a Salpeter IMF. The models evolve similarly up to redshifts of ~ 1. The differences in colour are likely due to the different treatment of the post main sequence stages and are discussed in **?**).

Following the predictions of these models, the limiting magnitudes in the near-IR wave-bands have been chosen to be 19.5 mag in K' and 21.0 mag in J, such that early-type objects having luminosities of $\gtrsim 0.5L^*$ at the present epoch can be detected in K' virtually at any redshift, and in J up to a redshift of $z \lesssim 1.5$, assuming passive evolution.

This is in agreement with the findings of the CFRS, which has shown that, while the luminosity function of the population of blue field galaxies shows significant signs of evolution in the redshift range $0.2 < z < 1$ – explainable by brightening or increase in space density – the redder part of the population (roughly redder than Sbc) shows no signs of evolution of its luminosity function in the same redshift range (**?**). The latter is interpreted in terms of brightening of the individual galaxies through passive evolution counterbalanced by negative density evolution, such that the luminosity function of the early-type population effectively does not evolve.

2.3 Field selection

The MUNICS survey consists of two sets of near-IR target fields, one set of single camera pointings having an effective field of view of $6' \times 6'$ pointed towards quasars, and a second set of $28' \times 13'$ fields constructed from mosaics of pointings targeted at random high Galactic latitude fields. This second set of fields was selected to contain no bright stars, nearby bright galaxies, and known nearby clusters of galaxies, and furthermore, to have low Galactic reddening (which is all together difficult to accomplish together with the prerequisite of having no bright star within the field, given our field size).

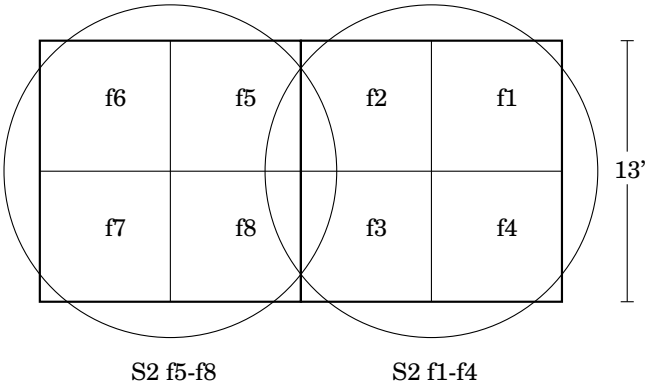

Figure 2. Layout and nomenclature of one of the MUNICS 'mosaic fields'. The size of the stripe is $13' \times 28'$, covered by 2×4 pointings in the near-IR and two pointings in the optical with the circular field of view of CAFOS (see text). The IR image is divided for technical reasons into two 2×2 mosaics. Each optical frame and IR mosaic frame are denoted by the name of the stripe, here S2, followed by the subfields they cover, giving S2 f1…f4 and S2 f5…f8 for this stripe.

A total of 16 fields targeted towards quasars with redshifts $0.5 < z < 2$ were observed. These fields will be referred to as 'quasar fields' hereafter, labelled Q1…Q16. The quasars were selected from the seventh edition of the **?**) catalogue. The selection criteria were $B < 19.0$ mag, $0^\circ < \mathrm{Dec} < 65^\circ$, $0^\mathrm{h} < \mathrm{RA} < 18^\mathrm{h}$, and $0.5 < z < 2$. Six of these quasars are not detected in the radio bands of the catalogue (6 cm and 11 cm) and are therefore considered radio quiet. The remaining 10 are radio loud.

A second set of 7 fields was targeted at high Galactic latitude 'empty' fields, i.e. free of bright stars ($V < 17$ mag) and known nearby extragalactic objects. These fields will be called 'mosaic fields' hereafter, for they are mosaiced images in the near-IR. They are labelled S1…S7. Each such field is laid out as a stripe of 4×2 IR pointings, yielding an area of $28' \times 13'$. For technical reasons, namely that four near-IR pointings can be completed in K' and J during a single night as well as image size and efficiency of optical follow-up observations (see below), each such stripe is divided into two 2×2 mosaics of single IR frames, denoted f1–f4 and f5–f8. This particular geometry was chosen for efficiency since such a 2×2 mosaic of IR frames suits the circular field of view of the optical imager we used (CAFOS, having a diameter of roughly 16 arcmin; see Section 3.2). For clarity, Fig. 2 shows a sketch of the geometry and nomenclature of the mosaic fields.

Finally, Table 1 lists the coordinates, available pass-bands, seeing, and Galactic foreground extinction of the observed mosaic and quasar fields.

2.4 Photometric system

The MUNICS imaging observations were carried out partly using non-standard filters, or imperfect realisations of standard filters (see Section 3 below). Since the colours of objects in the MUNICS cata-

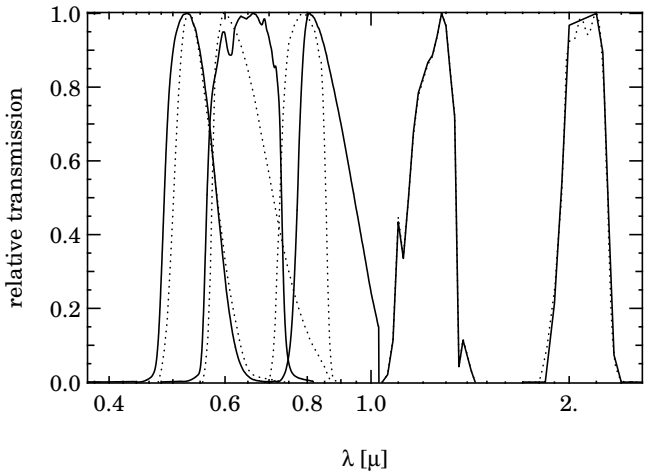

Figure 3. Relative transmission of MUNICS V, R, I, J, and K' filter (solid curves) curves including quantum efficiency of the CCD (V,R, and I) and Rockwell HAWAII near-IR array (J and K'), as well as the atmospheric transmission in the near-IR. Relative transmission curves of standard Johnson-Kron-Cousins V, R, and I filters, as well as J and K' are shown for comparison (dotted curves).

logues extend to much redder colours than any available photometric standard stars, we decided to work in the MUNICS instrumental photometric system and not to transform magnitudes into the standard Johnson-Kron-Cousins system. Linear transformation to the Johnson-Kron-Cousins system would have caused magnitude errors up to 1 mag, because the true transformations are highly non-linear, especially for red objects. The MUNICS photometric zero-points are in the Vega system.

Note that, since comparison of the object's colours with spectral synthesis models is intended (e.g. for deriving photometric redshifts or discussing the nature of EROs), it is important that the observed colours and the synthetic colours are consistent with respect to the filter set.

Accurate measurements of the transmission curves of the glass filters and quantum efficiencies of the detectors were obtained and applied in all subsequent synthetic photometry. The filter curves are shown in Fig. 3.

Such accurate knowledge of the filter system allows a reliable calibration of different bands via colour–colour diagrammes of stars which are compared with synthetic stellar sequences obtained from the convolution of SEDs from stellar libraries with the transmission curves. The absolute photometric zero-points can then be derived from a single photometric observation in one band only.

Fig. 4 shows a comparison of $R-J$ vs. $V-R$ and $J-K$ vs. $R-I$ colours derived by convolving stellar SEDs with the MUNICS filter curves with a sample of stars detected in the MUNICS mosaic fields. The stellar SEDs used for computing the synthetic colours are taken from the Bruzual-Persson-Gunn-Stryker spectral library (**?**; **?**), covering spectral types O5 to M8. The agreement between the synthetic photometry and the data along the stellar loci in colour–colour space demonstrates that the constructed filter curves match the actual ones and that the photometric zero-points are mutually consistent in the optical and the near-IR regime (see also Sect. 3.2 and Sect. 3.1). It is worth noting that we have no cool giants or supergiants in the MUNICS sample (as those would occupy the redder sequence in $J-K$ at $R-I \gtrsim 1.5$) and no stars of earlier type than roughly late F to G.

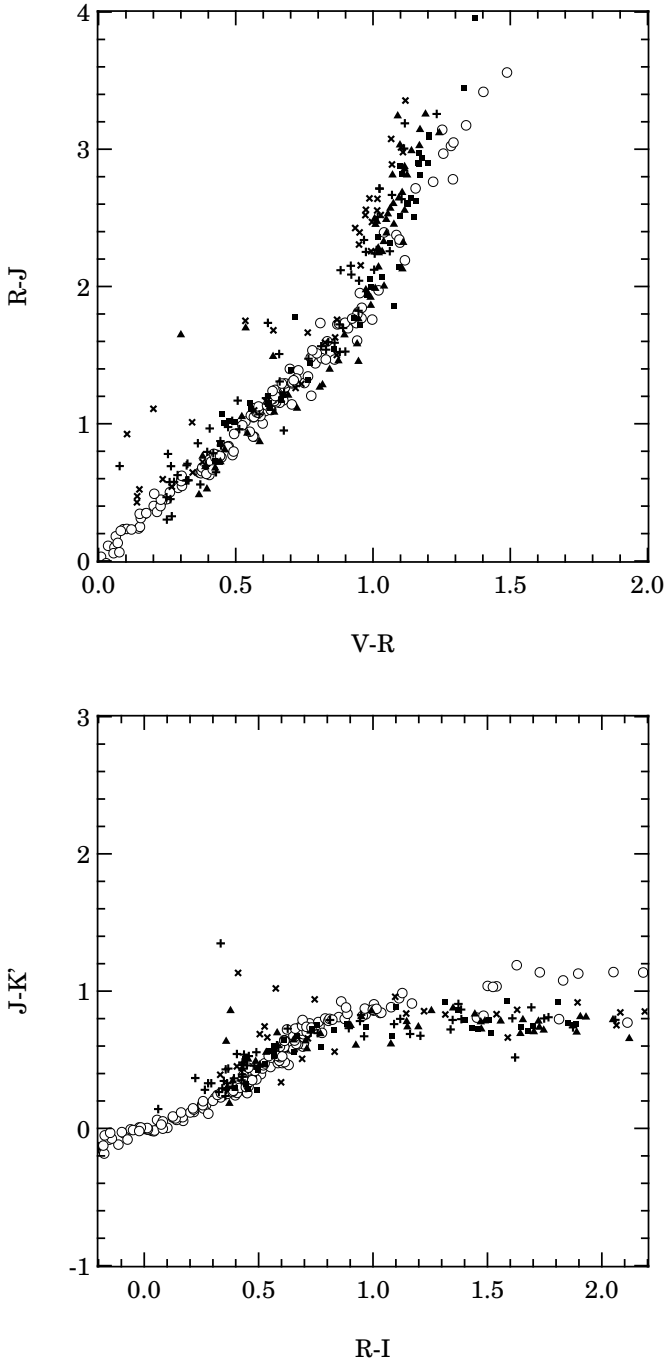

Figure 4. Comparison of $R-J$ vs. $V-R$ (upper panel) and $J-K$ vs. $R-I$ (lower panel) colours derived by convolving stellar SEDs (see text) with the MUNICS filter curves (open circles) with a sample of bright stars ($R < 21$) identified in the MUNICS fields S2 f1–f4 (crosses), S4 f1–f4 (x), S6 f5–f8 (squares), and S7 f5–f8 (triangles).

3 OBSERVATIONS AND DATA REDUCTION

3.1 Infrared observations and data reduction

The K'-band and J-band imaging was obtained using the Omega-Prime camera (**?**) at the prime focus of the Calar Alto 3.5-m telescope. Omega-Prime is equipped with a HAWAII 1024^2 HgCdTe array. The image scale is 0.396 arcsec per pixel, resulting in a $6.75' \times 6.75'$ field of view. The K' filter ($\lambda_0 = 2.12\mu$, $\Delta\lambda =$

Table 1. The MUNICS mosaic and quasar fields

Field	Mosaic/QSO	z_{QSO}	α (J2000)	δ (J2000)	Filters	K' seeing	$E(B-V)$	Remarks
S1	f1–f2		14:49:25	+65:55:31	KJIRV	$1.01''$	0.017	(1)
S2	f1–f4		03:06:41	+00:01:12	KJIRV	$1.30''$	0.080	(3)
	f5–f8		03:06:41	−00:13:30	KJIRV	$1.17''$	0.083	(3)
S4	f1–f4		03:15:00	+00:07:41	KJIRV	$0.95''$	0.094	(3)
	f5–f8		03:14:05	+00:07:41	KJIRV	$2.52''$	0.094	(2)
S3	f1–f4		09:04:38	+30:02:56	KJIRV	$1.10''$	0.025	(3)
	f5–f8		09:03:44	+30:02:56	KJIRV	$1.11''$	0.027	(3)
S5	f1–f4		10:24:01	+39:46:37	KJIRV	$1.17''$	0.012	(3)
	f5–f8		10:25:14	+39:46:37	KJIRV	$1.32''$	0.009	(3)
S6	f1–f4		11:55:58	+65:35:55	KJIRV	$1.21''$	0.019	(3)
	f5–f8		11:57:56	+65:35:55	KJIRV	$1.41''$	0.015	(3)
S7	f1–f4		13:33:41	+16:51:44	KJ	$1.68''$	0.023	(2)
	f5–f8		13:34:44	+16:51:44	KJIRV	$1.12''$	0.029	(3)
Q1	J000701.3+002242	0.87	00:07:01	+00:22:42	KJIR	$1.39''$	0.073	PB 5741; (4)
Q2	J000750.9+031733	1.10	00:07:51	+03:17:32	KJIR	$1.07''$	0.020	PB 5753; (4)
Q3	J005444.0+144646	0.91	00:54:44	+14:46:47	KJIR	$1.30''$	0.054	PHL 892; (4)
Q4	J005905.6+000651	0.72	00:59:06	+00:06:52	KJIR	$1.00''$	0.027	PHL 923
Q5	J010026.8+043941	0.53	01:00:27	+04:39:41	KJIR	$1.06''$	0.024	UM 81; (4)
Q6	J011033.7+015446	0.71	01:10:35	+01:55:37	KJIR	$1.29''$	0.028	MS 01080+0139; (4)
Q7	J011818.5+025806	0.67	01:18:19	+02:58:06	KJIR	$1.23''$	0.039	3C 37
Q8	J015838.9+034744	0.66	01:58:39	+03:47:43	KJIR	$1.23''$	0.031	UM 153; (4)
Q9	J025937.5+003736	0.53	02:59:38	+00:37:37	KJIR	$1.33''$	0.090	US 3472
Q10	J115517.9+653917	1.20	11:55:28	+65:38:10	KJIRV	$1.62''$	0.017	4C 65.13
Q11	J122033.9+334312	1.51	12:20:34	+33:43:10	KJ	$1.22''$	0.012	3C 270.1
Q12	J133335.8+164904	2.08	13:33:40	+16:48:14	KJ	$1.86''$	0.022	PB 3977
Q13	J133411.6+550125	1.25	13:34:12	+55:01:25	KJ	$1.59''$	0.007	4C 55.27
Q14	J135704.5+191906	0.71	13:57:05	+19:19:07	KJ	$1.72''$	0.060	PKS 1354+19
Q15	J135817.6+575205	1.38	13:58:18	+57:52:05	KJ	$1.89''$	0.010	4C 58.29
Q16	J171938.4+480413	1.08	17:19:38	+48:04:13	KJ	$1.79''$	0.019	PG 1718+481

Field coordinates are given with respect to the image centres.
QSO designations according to **?**).

(1) Mosaic incomplete in the near-IR.
(2) Near-IR data quality poor.
(3) Good data quality in all five wave-bands.
(4) Radio quiet QSO.

0.35μ; see **?**) was used because it significantly reduces the thermal background seen by the detector relative to the standard K filter, thus gaining sensitivity. Table 2 lists all observing runs undertaken to present date.

The K'-band data were observed using a dithering pattern consisting of 16 positions within an area of $30'' \times 30''$laid out on a 4×4 grid with $10''$spacing between adjacent grid points. The data were recorded using a randomized sequence of these 16 positions.

On each position 28 seconds of net exposure time were collected, divided into several shorter exposures as necessary depending on the ambient temperature and thus the level of the thermal background. The length of the single exposures was always chosen such that non-linearity of the detector was negligible.

This 16 position cycle was repeated 3 times yielding 48 frames and a total exposure time of 1344 s. The J-band images were observed using the same dithering pattern with longer integration times of 80 s on each position and therefore needed only one cycle, giving a total of 1280 s.

The near-IR mosaic fields consist of four such Omega-Prime pointings arranged in a 2×2 configuration with $6'$ offset in each direction measured from field centre to field centre. Each mosaic then covers a total area of 162 square arc minutes, counting only the central area with the longest total exposure time and removing overlaps and borders due to the dithering pattern (see Fig. 2).

On photometric nights, standard stars from the UKIRT Faint IR Standard Stars catalogue (**?**) were observed several times during the night at different air masses to determine the photometric zero point and the atmospheric extinction coefficient. To increase the number of standard star measurements available for each night, the calibrations of further stars in the UKIRT fields by **?**) were included. Night-to-night variations in the zero-point were typically less than 0.1 mag. Targets observed during non-photometric nights were re-observed (with shorter exposure time) at least once during photometric conditions to assure accurate photometric calibration. The typical formal uncertainties in the zero-points were 0.05 mag in K' and 0.06 mag in J. The extinction coefficients were found to be stable for all runs with typical values around 0.08 ± 0.025 mag per airmass in K' and 0.12 ± 0.02 mag per airmass in J. By comparison with synthetic photometry as explained in Sect. 2.4 we conclude that additional systematic errors in the near-IR calibration as well as systematic offsets between the near-IR and the optical wave-bands cannot be larger than ~ 0.1 mag.

The data were reduced using standard image processing algo-

Table 2. MUNICS observing runs

Date	Tel.	Instrument	Remarks
1996 24-27.10	CA35	Ω'	Quasar fields
1997 15-19.5	CA35	Ω'	Quasar fields
1998 8-14.4	CA35	Ω'	
1998 12-17.5	CA35	Ω'	
1998 28.5-1.6	CA22	CAFOS	
1998 16-18.11	McD27	IGI	Quasar fields
1998 16-20.12	CA22	CAFOS	
1998 23-30.12	CA35	Ω'	
1999 18.3	Wdst	MONICA	Calibrations
1999 27.5-3.6	CA35	Ω'	
1999 9-18.6	CA22	CAFOS	
2000 26-31.5	CA35	MOSCA	Spectroscopy
2000 27-28.5	HET	LRS	Spectroscopy
2000 16.7	CA35	Ω'	(1)
2000 20-22.11	ESO-VLT	FORS1/2	Spectroscopy
2000 24-28.11	CA35	MOSCA	Spectroscopy
2000 5.12	CA22	CAFOS	(1)
2000 17-18.12	CA22	CAFOS	(1)
2000 19.12	CA35	Ω'	(1)
2001 17-21.1	CA35	MOSCA	Spectroscopy
2001 11-13.2	CA35	Ω'	(1)

(1) Re-imaging of fields with poor data quality.

CA22 and CA35 are the 2.2-m telescope and the 3.5-m telescope of Calar Alto Observatory, respectively. McD27 is the 2.7-m telescope and HET is the Hobby-Eberly Telescope, both of McDonald Observatory, Austin, Texas. Wdst is the 0.8-m telescope of Wendelstein Observatory operated by the Universitäts-Sternwarte München.

rithms within IRAF*. For each frame a sky frame was constructed from typically 6 to 12 (temporally) adjacent frames where bright objects and detector defects have been masked out, and which were scaled to have the same median counts. These frames were then median-combined using clipping to suppress fainter sources and otherwise deviant pixels to produce a sky frame. The sky frame was scaled to the median counts of each image before subtraction to account for variations of sky brightness on short time-scales. The sky-subtracted images were flat-fielded using dome flats to remove pixel-to-pixel fluctuations in quantum efficiency. The frames were then registered to high accuracy using the brightest ~ 10 objects and finally co-added, again using clipping to suppress highly deviant pixels due to cosmic ray events and defective pixels on the array, after being scaled to airmass zero and to a common photometric zero-point.

The 2×2 mosaic images were produced by registering the images using objects in the overlap regions, simultaneously cross checking the photometric calibration. Before combining, the images were adjusted to have the same background counts computed from the mode of the pixel values in 'empty' sky regions of the images to correct for residual differences in sky brightness. Absolute astrometric calibration of the images is discussed in Sect. 3.3 below.

* IRAF is distributed by the National Optical Astronomy Observatories, which are operated by the Association of Universities for Research in Astronomy, Inc., under cooperative agreement with the National Science Foundation.

3.2 Optical observations and data reduction

Optical imaging of the mosaic fields was performed at the Calar Alto 2.2-m telescope in the V, R, and I bands using the Calar Alto Faint Object Spectrograph (CAFOS) focal reducer in direct imaging mode. CAFOS was equipped with a SITe 2048^2 CCD detector, yielding a resolution of 0.53 arcsec per pixel and a circular field of view (due to vignetting by optics) of $16'$ in diameter. The V-band filter used was a standard Johnson filter, the R-band filter was an R_2 filter ($\lambda_0 = 0.648\mu$, $\Delta\lambda = 0.168\mu$), slightly narrower and bluer than Kron-Cousins R. The I-band filter was an RG780 filter with the red cutoff set by the CCD (see Fig. 3.) Total exposure times were 2700 s in V and I, and 1800 s in R, divided into several shorter exposures taken with offsets of $\sim 15''$, depending on the presence of bright stars and on seeing conditions to avoid too many saturated objects.

The quasar fields were imaged using the Imaging Grism Instrument (IGI) at the 2.7-m telescope of McDonald Observatory, using a 1024^2 TK4 CCD ($7'$ field of view) and Mould R and I interference filters. Exposure times 1800 s in R and 2700 s in I, again divided into several shorter exposures.

The optical CCD data were reduced in a fairly standard manner using IRAF, except for cosmic ray cleaning. The frames were bias/overscan corrected and then flat-fielded using a combination of dome flats and sky flats. The I-band frames showed considerable fringing. Fringe images were created from the affected series of science exposures and occasionally also from twilight flats by medianing de-registered images after masking bright sources by hand as necessary. In some cases it was necessary to subtract a low order fit to the overall background in the science frames prior to construction of the fringe image to account for changes in the illumination pattern present in the images in the case where a bright star was close to the image border. The fringe images were then appropriately scaled and subtracted from the affected frames.

Cosmic ray events were identified by searching for narrow local maxima in the image and fitting a bivariate rotated Gaussian to each maximum. A locally deviant pixel is then replaced by the mean value of the surrounding pixels if the Gaussian obeys appropriate flux ratio and sharpness criteria (**?**). Such a procedure is much more expensive in terms of computing time (roughly 10 CPU minutes per frame) compared to standard median filtering techniques, but is much more reliable in finding cosmic ray events in the wings of objects and in cleaning long cosmic ray trails.

The re-imaging system of CAFOS causes substantial radial distortion of the image which had to be dealt with before co-adding the offset images. Therefore the frames were rectified using the known distortion equation, a polynomial of fourth order in the distance from the optical axis (K. Meisenheimer, private communication).

If necessary, variations in the background intensity across the frames caused by scattered light were fitted and subtracted in each individual frame. The images were then corrected for atmospheric extinction and scaled to a common photometric zero-point before finally being added using the positions of ~ 15 bright objects for determination of the offsets between the individual frames.

During photometric nights, photometric standard stars were observed (**?**; **?**) and programme fields with insecure calibrations were re-observed with short exposures. The run at the Wendelstein 0.8-m telescope was devoted to such re-calibration to have independent calibrations for the fields. For each field, a photometric zero point and the atmospheric extinction were determined. No colour terms were fitted to the calibration data, as explained in Sect. 2.4.

The typical formal uncertainties in the photometric calibration were ~ 0.08 mag in I, ~ 0.04 mag in R, and ~ 0.05 mag in V. The extinction coefficients were usually consistent with a Rayleigh atmosphere, with a few nights showing higher extinction, albeit within the variations typical for Calar Alto. As with the near-IR observations, consistency was checked against synthetic colours of stars, again finding no systematic offsets. We conclude that systematic errors in the optical photometric calibration are again smaller than 0.1 mag in all filters.

3.3 Astrometry

Astrometric solutions were computed for all K'-band images to translate pixel coordinates into celestial coordinates. For this purpose, astrometric standards from the USNO-SA1.0 catalogue (**?**) were selected in each frame. The celestial coordinates of these stars were matched against the pixel position using the IRAF task CCXYMATCH, and the plate solution was computed using CCMAP. The typical scatter is less than 0.4 arcsec rms.

The V, R, I, and J images of each field were registered against the K'-band image by matching the positions of ~ 200 bright homogeneously distributed objects in the frames and determining the coordinate transform from the K'-band system to each image in the other four pass-bands using the tasks XYXYMATCH and GEOMAP within IRAF. The scatter in the determined solutions is less than 0.1 pixels rms in the transformation from K' to J, and less than 0.2 pixels rms from K' to the optical frames. Note that the frames themselves are not transformed. We only determine accurate transformations and apply these later to the apertures in the photometry process.

3.4 Spectroscopy

A spectroscopic follow-up programme is currently being conducted at the Calar-Alto 3.5-m telescope, the Hobby-Eberly Telescope, and the VLT, aiming ultimately at a magnitude-limited redshift survey of the K'-band selected catalogue. The results of these observations will be discussed in a future paper. In the mean time, the spectroscopic redshifts are used to calibrate photometric redshifts.

4 DATA ANALYSIS

The construction of photometric catalogues from the reduced images will be discussed in this chapter. The individual steps in this process will be described in some detail. These include the detection of objects in the K'-band images (see Sect. 4.1), a first analysis of the survey's completeness (Sect. 4.2), the photometry of objects in all filters (see Sect. 4.3), and the separation of stars and galaxies in the catalogue (see Sect. 4.4). The chapter will be concluded by a comparison of number counts for galaxies with previous studies (Sect. 4.6) as a further consistency check on our data set.

4.1 Object detection

Object detection was performed using the YODA source extraction software (**?**). This package was specifically designed to be used in multi-band imaging surveys, where the background noise is often inhomogeneous across the images – in mosaiced frames or in dithered images where the exposure time is a function of position – and where the frames do not share a common coordinate system and pixel scale, due to the use of multiple telescopes and imagers. The second point was considered a serious problem since re-sampling the images to a common coordinate system introduces quite considerable noise for faint sources.

Sources are detected by requiring a minimum number N_{pix} of consecutive pixels to lie above a certain threshold t expressed in units of the local rms σ of the background noise. To foster detection of faint sources, the images are convolved with a Gaussian of FWHM equal to the seeing in the image. The choice of the number of consecutive pixels N_{pix} and the threshold t is somewhat a trade-off between limiting magnitude at some completeness fraction, say 50 per cent, and the number of tolerable spurious detections per unit image area (**?**). Note that, since we aim at purely K'-band selected catalogues for most of our applications, the presence or absence of a source in other wave-bands cannot be used for confirmation or rejection of sources, so the expected number of spurious detections per unit image area is of great interest to us.

To find reasonable values for N_{pix} and t we performed simulations on the K'-band image of one of our mosaic fields (S6 f5–f8). The dependence of the 50 per cent completeness limit on N_{pix} and t was determined by adding point sources to the K'-band image and recording the fraction of the objects recovered by the detection software as a function of N_{pix} and t. The number of false detections was determined by looking for positive detections in an inverted (multiplied by -1) version of the image, after convincing ourselves that the background noise was sufficiently well approximated by a Gaussian. Fig. 5 shows the results of these tests.

At the depth of our data we detect roughly 1000 objects per mosaic field. Accepting 1 per cent contamination by false detections, i.e. roughly 10 false objects per mosaic field we fixed the detection threshold at $t = 3\sigma$ and the minimum number of consecutive pixels at 1.4 times the seeing disk area, $N_{pix} = 1.4\pi(\mathrm{FWHM}/2)^2$, (10 pixels at $1''$, 16 pixels at $1.5''$seeing for the near-IR frames) and performed object detection using these parameters on all K'-band images.

4.2 Completeness

To estimate the completeness limits of the MUNICS K'-selected catalogues, Monte–Carlo simulations were carried out to determine the detection completeness as a function of magnitude in each K'-band image.

In these simulations, 250 artificial objects with a Moffat-type PSF having the same FWHM as stars in the frames were added to the MUNICS images. For this purpose the IRAF package ARTDATA was used. A constant distribution of apparent magnitudes of the artificial objects was applied. Then the object detection algorithm was run on these frames, and the number of re-detected objects was recorded as a function of magnitude. This procedure was repeated 250 times in order to decrease statistical errors.

Fig. 6 shows the results of these simulations for 6 of the mosaic fields where imaging data in all five colours are available. The 50 per cent and 90 per cent completeness limits of the K'-band images are listed in Table 3. From these simulations we conclude that the mosaic fields comprise a reasonably homogeneous data set, with field-to-field variations in 50 per cent completeness of order ~ 0.4 mag, with the exception of S6 f1–f4 which is considerably shallower. The quasar fields, which are not shown here, have completeness levels in the same range as the shown mosaic fields.

Simulations with extended objects having de Vaucouleurs and exponential surface brightness profiles have also been performed.

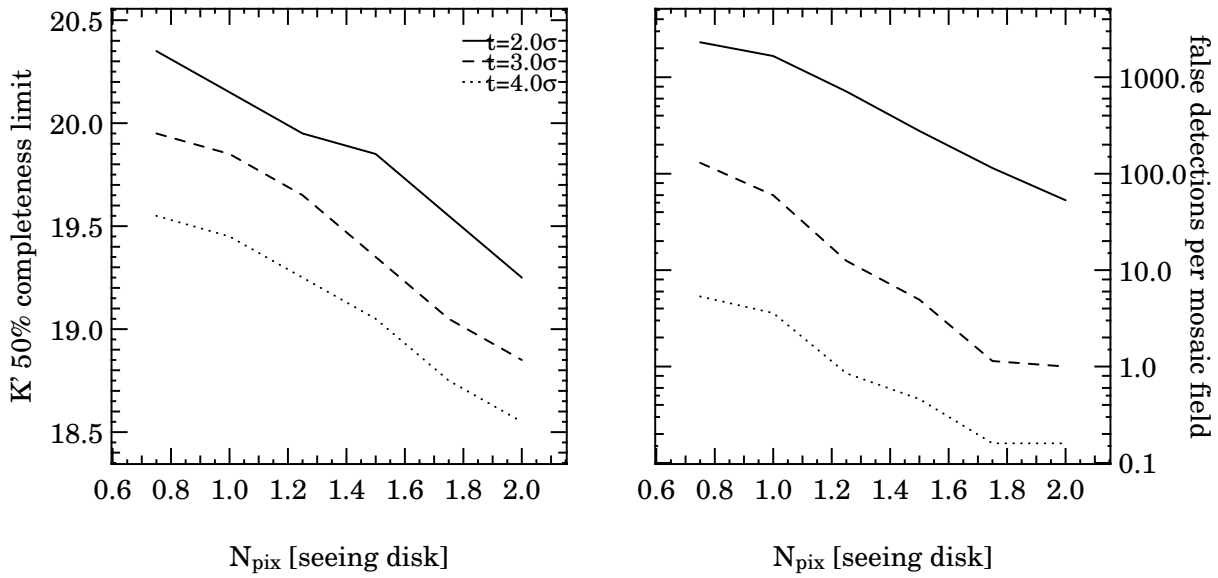

Figure 5. The behaviour of the 50 per cent completeness limit for point-like sources and the number of spurious source detections as a function of the detection threshold t in units of the local background rms σ and the required number N_{pix} of consecutive pixels above the threshold in units of the seeing disk area $\pi(\mathrm{FWHM}/2)^2$. The *left panel* shows the change in limiting magnitude at 50 per cent completeness as a function of N_{pix} for detection thresholds of 2.0σ (solid line), 3.0σ (dashed line), and 4.0σ (dotted line). The *right panel* shows the number of spurious sources integrated over all magnitudes per image (one mosaic field), again as a function of N_{pix} and the detection threshold t. Line styles as in the left panel.

Table 3. Completeness limits for the MUNICS mosaic fields

	S2 f1–f4		S4 f1–f4		S5 f1–f4		S6 f1–f4		S6 f5–f8		S7 f5–f8	
Band	90%	50%	90%	50%	90%	50%	90%	50%	90%	50%	90%	50%
K	19.05	19.45	18.69	19.18	19.42	19.80	18.26	18.56	19.53	19.92	19.23	19.83
J	20.29	20.68	20.62	21.04	20.53	20.93	20.06	20.44	20.69	21.06	20.84	21.39
I	21.86	22.29	22.18	22.60	21.72	22.07	22.35	22.72	21.70	22.08	21.94	22.34
R	22.78	23.21	23.18	23.50	22.94	23.32	23.25	23.58	22.95	23.37	22.88	23.28
V	23.13	23.51	23.62	23.94	23.36	23.72	23.36	23.68	23.50	23.89	22.96	23.28

In general they yield 50 per cent completeness limits between 0.5 and 1 magnitude brighter than those determined for stellar sources, depending mostly on the adopted profile scale-length. The full results of these simulations will be extensively discussed in a future paper in the context of surface-brightness selection effects.

4.3 Photometry

Photometry was performed in elliptical apertures the shape of which were determined from the first and second moments of the light distribution in the K'-band image, as described in **?**), and additionally in fixed size circular apertures of 5 and 7 arc seconds diameter. To ensure measurement at equal physical scales in every pass-band, the individual frames were convolved to the same seeing FWHM, namely that of the image with the worst seeing in each field. The signal-to-noise ratio as a function of magnitude for the $5''$apertures is shown in Fig. 7. At the 50 per cent completeness limit in the K' band (19.59), the signal-to-noise ratio is ~ 10. For such an object having an $R-K'$ colour of 6, the signal-to-noise ratio in the R band is roughly 3.

Aperture fluxes and magnitudes were computed for each object present in the K'-band catalogue irrespective of a detection in any other band. For this purpose the centroid coordinates of the sources detected in the K'-band images were transformed to the other frames using the full astrometric transformations as determined in Sect. 3.3. The shape of the apertures were transformed using only the linear terms of the transformation.

The photometric accuracy for the $5''$aperture magnitudes is roughly 0.1 mag at $K' = 19$ mag. This error estimate includes the effects of photon noise and uncertainty in background determination and subtraction, but does not include (systematic) errors due to the photometric calibration. Fig. 8 shows plots of the magnitude error vs. object magnitude for one mosaic field in all five pass-bands.

4.4 Star-galaxy separation

Star–galaxy separation relies on YODA's image classification stage which is based on a Bayesian analysis of the probability that an object's light distribution is due to an unresolved (point-like) source by comparison with light distributions constructed from the image's PSF. YODA's classification parameters are calculated for all objects in the catalogue in all available pass-bands.

As demonstrated in **?**), classification is reliable across wavebands and imaging instruments, and stellar sources almost do not scatter out of the stellar locus in parameter space (except in the presence of crowding). Rather, images of faint galaxies as they become smaller at larger distances, move onto the locus of point-like sources.

Using the multi-pass-band information available in MUNICS allows us to push the limit of reliable classification by using

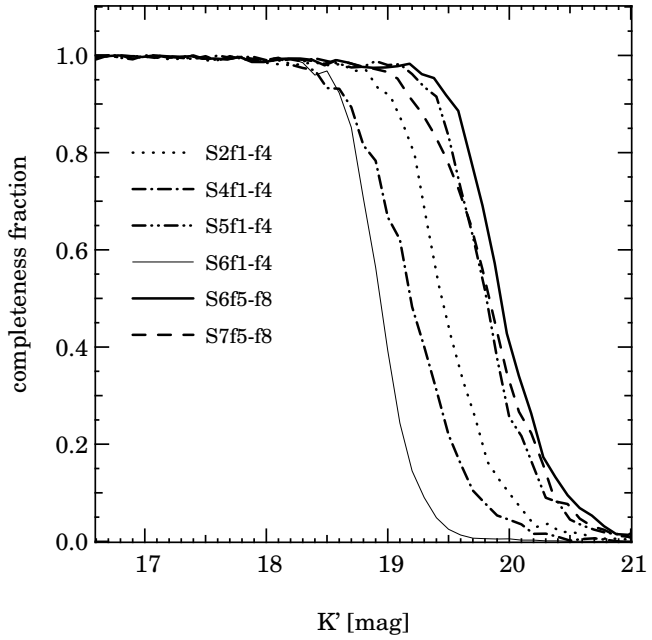

Figure 6. Completeness fraction of point-like sources as a function of magnitude in the K'-band mosaic fields as determined by adding Moffat-type objects to the images and recording the fraction of such objects that was recovered by the detection process.

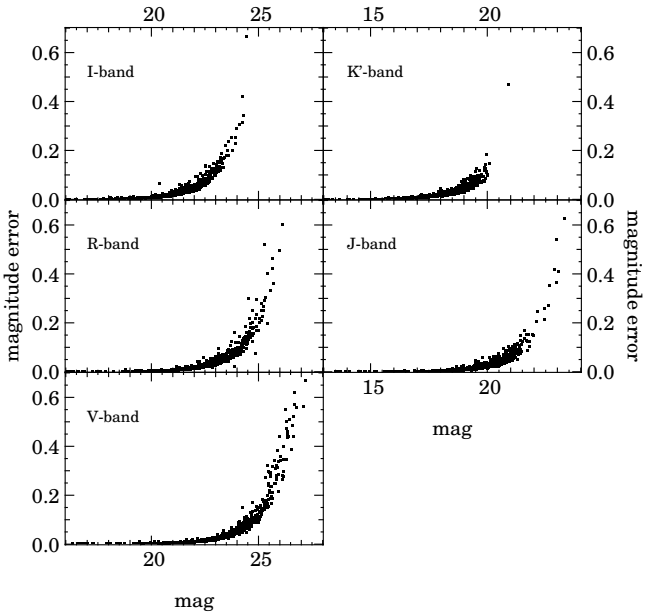

Figure 8. Magnitude errors as a function of magnitude in the mosaic field S6 f5–f8 in K', J, I, R, and V as measured in circular apertures of $5''$diameter for K'-band selected objects. Aperture fluxes are measured in every pass-band for each object present in the K'-band catalogue irrespective of a detection in any other band.

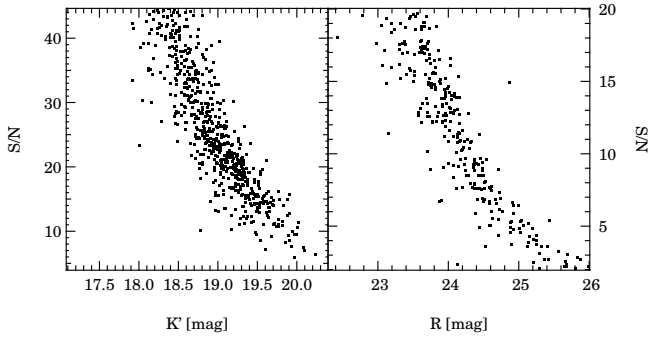

Figure 7. Signal-to-noise ratio in K' (left panel) and R (right panel) as a function of magnitude in circular apertures of $5''$diameter for objects taken from the K'-selected catalogue of the field S6 f5–f8. The signal-to-noise ratio is defined here as the signal-to-noise ratio of the aperture photometry, i.e. total (sky-subtracted) flux within the aperture divided by the total noise within the aperture, with contributions to the latter coming from Poisson fluctuations in the object as well as the background, and the error in the determination of the background.

for each object the classification information in those pass-bands where the signal-to-noise ratio is highest. Therefore, in the mosaic fields where 5 colours are available, we classify as stellar every source that is classified as stellar by YODA in the three pass-bands with highest signal-to-noise. In the quasar fields, where less colour information is available, we rely on the two images with highest signal-to-noise.

As can be seen in Fig. 10, objects classified as stars occupy the clearly defined stellar sequence in the $R-J$ vs. $J-K'$ colour-colour plane, with only very few objects classified as stellar having a $J-K'$ colour redder than $\sim$ 1. These are either misclassified faint and compact galaxies or very late-type stars or brown dwarfs, the latter is a possibility for those objects having also red $R-J$ colour. The objects lying on the stellar sequence at $R-J \gtrsim 2$ and which are classified as galaxies were found to be faint and barely resolved objects failing the classification as a star only due to their appearance in one filter. In many cases an obvious reason – like a second close object – could be identified. We conclude that most of these objects are, in fact, misclassified stars. The total fraction of point-like sources in the catalogues is ~ 10 per cent.

We have also checked the results of the image-based classification against spectral classification for those objects where spectroscopy was already available, namely 45 galaxies and 53 stars having $R < 20.5$. All these objects were correctly classified.

4.5 Galactic extinction

We use the Galactic reddening maps provided by **?**) using a value of $R_V = 3.1$ to calculate $A_\lambda = R_\lambda E(B-V)$ to correct the measured magnitudes for Galactic foreground extinction. The values of $E(B-V)$ for our fields are given in Table 1.

4.6 Galaxy number counts

In Table 4 we present number counts of galaxies in the MUNICS mosaic fields in all five filters K', J, I, R, and V. These counts are also shown in fig. 9, together with a compilation of number counts from the literature. Object catalogues were generated independently for each pass-band for this purpose, and star–galaxy separation is based on the PSF classification as described above, using only single pass-band information. The data were not transformed into the standard magnitude system for this comaprison. Completeness corrections were not applied to these galaxy number counts, but corrected counts will be presented in the context of a more detailed completeness analysis in a future paper. The counts are average counts from all the available MUNICS mosaic fields, with

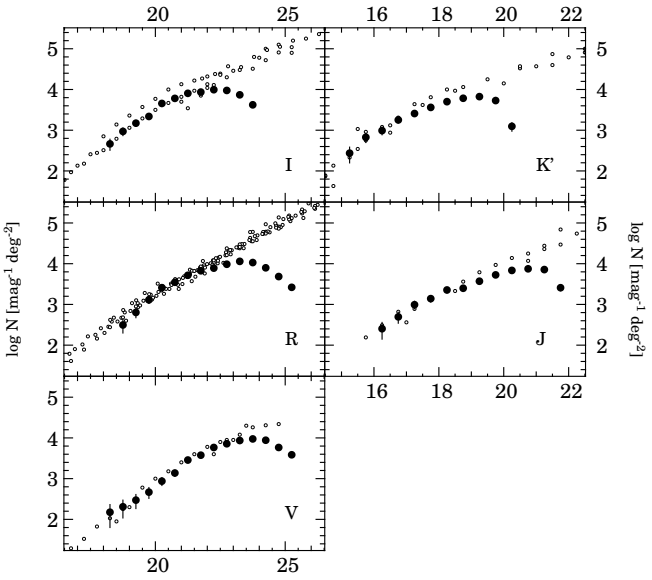

Figure 9. Number counts for galaxies in K', J, I, R, and V from MUNICS data (filled circles) and previous studies (open circles), as described in the text. The counts shown are average number counts from all available MUNICS data and have not been corrected for incompletness. Error bars indicate Poisson errors.

field-to-field variations in the number counts being on the level of 0.1 dex. The errors given in Table 4 only include Poissonian errors.

The number counts are compared to the following literature values. **?**; **?**; **?**; **?**; **?** for the K band, **?**; **?** for the J band, **?**; **?**; **?**; **?**; **?**; **?** for the I band, **?**; **?** for the R band, and **?**; **?**; **?** for the V band.

We generally find good agreement with previously published number counts in all pass-bands, again as a consistency check confirming the quality of our photometry.

4.7 Colour distributions and objects at $z \geq 1$

In Fig.10 we show the $J-K'$ vs. K' colour–magnitude diagramme and the $R-J$ vs. $J-K'$, $V-I$ vs. $J-K'$, and $V-I$ vs. $V-R$ colour–colour diagrammes for MUNICS data from three mosaic fields. The total number of objects shown is 2977, of which 286 are classified as point-like. These plots also contain the tracks defined by the stellar population synthesis models described in detail in Sect. 2.2. Briefly, the models are an SSP, and three exponential star formation histories with e-folding times of 1, 3, and 10 Gyr forming at $z = 4$. The models have been normalised such that they represent typical L^* objects at $z = 0$, with L^* chosen according to their 'photometric' Hubble type. The cosmology adopted is again $H_0 = 65, \Omega_0 = 0.3, \Omega_\Lambda = 0.7$.

These models reasonably envelope the region in the colour–magnitude $J-K'$ vs. K' plane occupied by the data, with the SSP model following the outline of the data points along the bright and red edge as might be expected since any further star formation or a later formation epoch would render the object bluer relative to the SSP.

It is also worth noting that the models constitute a continuous sequence with the duration of the star formation as the parameter in the $R-J$ vs. $J-K'$ plane, closely following the SSP track up to a redshift of ~ 1, then rapidly turning bluer in $R-J$ while still getting redder in $J-K'$. A significant fraction of objects between the SSP and the 1 Gyr track is compatible with being well evolved objects at a redshift $z \gtrsim 1$. How many objects exactly populate this region is an important question which will be addressed in a future paper.

We finally conclude from these diagrammes that the quality of our data meets the requirements expressed in Sect. 2 and that we are in a position to construct a catalogue containing a large number of massive field galaxies in the redshift range $0.5 \lesssim z \lesssim 1.5$ to study their evolution in detail.

5 SUMMARY

The Munich Near-IR Cluster Survey (MUNICS) is a wide-area, medium-deep, photometric survey selected in the K' band. It covers an area of roughly one square degree in the K' and J near-IR pass-bands with additional complementary optical imaging in the V, R, and I bands.

MUNICS has been undertaken to study the evolution of both field galaxies and galaxy clusters out to redshifts around unity, and to investigate the nature of extremely red objects and their connection to the population of massive field spheroidal galaxies.

The survey area consists of 16 $6' \times 6'$ fields targeted at QSOs with redshifts $0.5 < z < 2$ and 7 $28' \times 13'$ stripes targeted at 'random' high Galactic latitude fields. Ten of the QSO fields were additionally imaged in R and I, and 0.6 deg^2 of the randomly selected fields were imaged in the V, R, and I bands. The resulting object catalogues were strictly selected in K', having a limiting magnitude (50 per cent completeness) of $K' \sim 19.5$ mag and $J \sim 21$ mag, sufficiently deep to detect passively evolving early-type systems up to a redshift of $z \lesssim 1.5$ and luminosity of $0.5L^*$. The optical data reach a depth of roughly $R \sim 23.5$ mag. The project's main scientific aims are the identification of galaxy clusters at redshifts around unity and the selection of a large sample of field early-type galaxies at $0 < z < 1.5$ for evolutionary studies.

In this paper we describe the selection of survey fields as well as the observations and the reduction of the near-infrared and optical data. We define our photometric system and show it to be internally consistent by checking it against synthetic photometry of stars from stellar libraries. The construction of the K'-selected object catalogue is described in detail, particularly the choice of parameters for object detection, which ensures completeness to as faint magnitudes as possible while keeping the rate of false detections in our strictly K'-selected catalogue small. Photometry of the objects in the catalogue is performed in elliptical apertures on frames convolved to the same PSF in all filters, in order to guarantee measurements of the flux in equal physical areas. Stars and galaxies in the fields are classified using a Bayesian analysis of the light distribution in the images.

The quality of the survey data in terms of signal-to-noise ratio and limiting magnitude is discussed, with the completeness of the survey fields being characterised by Monte–Carlo simulations of point sources in the MUNICS frames. Also, galaxy number counts are presented in the five filters K', J, I, R, and V and compared to counts published by other authors.

Finally, we show the $J-K'$ vs. K' colour–magnitude diagramme and the $R-J$ vs. $J-K'$, $V-I$ vs. $J-K'$, and $V-I$ vs. $V-R$ colour–colour diagrammes for MUNICS objects, together with stellar population-synthesis models for different star-formation histories and conclude that the data set presented is suitable for extracting a catalogue of massive field galaxies in the red-

Table 4. K', J, I, R, and V-band galaxy number counts for the MUNICS mosaic fields. The counts as a function magnitude and the error of the counts are given in logarithmic units. The values have not been corrected for incompleteness. The errors are Poissonian errors only.

	K'			J			I			R			V		
mag	$\log n$	σ_{low}	σ_{high}	$\log n$	σ_{low}	σ_{high}	$\log n$	σ_{low}	σ_{high}	$\log n$	σ_{low}	σ_{high}	$\log n$	σ_{low}	σ_{high}
14.25	1.19	0.47	1.37												
14.75	2.11	1.38	2.32												
15.25	2.44	2.20	2.59												
15.75	2.83	2.70	2.93												
16.25	2.99	2.89	3.07	2.40	2.15	2.56									
16.75	3.25	3.18	3.32	2.69	2.54	2.81	2.14	1.61	2.34						
17.25	3.41	3.35	3.46	2.99	2.89	3.08	2.13	1.40	2.33						
17.75	3.56	3.51	3.61	3.14	3.06	3.21	2.38	2.15	2.53						
18.25	3.70	3.66	3.74	3.35	3.29	3.41	2.66	2.50	2.77	1.92	1.72	2.04	2.17	1.80	2.36
18.75	3.79	3.75	3.82	3.40	3.34	3.45	2.97	2.86	3.05	2.49	2.29	2.63	2.30	2.03	2.47
19.25	3.83	3.79	3.86	3.57	3.52	3.61	3.17	3.09	3.24	2.80	2.67	2.90	2.47	2.26	2.61
19.75	3.73	3.69	3.77	3.73	3.68	3.76	3.33	3.27	3.39	3.11	3.02	3.18	2.66	2.51	2.78
20.25	3.10	2.98	3.18	3.84	3.80	3.87	3.65	3.61	3.69	3.41	3.35	3.46	2.93	2.83	3.02
20.75				3.87	3.84	3.91	3.78	3.74	3.81	3.54	3.49	3.58	3.13	3.05	3.20
21.25				3.86	3.82	3.89	3.90	3.87	3.93	3.71	3.67	3.75	3.45	3.40	3.50
21.75				3.41	3.34	3.47	3.93	3.90	3.96	3.82	3.79	3.85	3.57	3.52	3.61
22.25							3.99	3.96	4.02	3.89	3.85	3.92	3.76	3.72	3.80
22.75							3.97	3.94	4.00	3.98	3.95	4.01	3.85	3.82	3.88
23.25							3.86	3.83	3.90	4.05	4.03	4.08	3.93	3.90	3.96
23.75							3.62	3.57	3.66	4.02	4.00	4.05	3.97	3.94	4.00
24.25							3.36	3.29	3.41	3.89	3.86	3.92	3.94	3.91	3.97
24.75							2.75	2.58	2.86	3.68	3.64	3.72	3.76	3.72	3.80
25.25										3.42	3.36	3.47	3.58	3.53	3.62
25.75										3.03	2.93	3.11	3.16	3.06	3.23

shift range $0.5 \lesssim z \lesssim 1.5$ for evolutionary studies and follow-up observations.

ACKNOWLEDGEMENTS

The authors would like to thank the staff at Calar Alto Observatory and McDonald Observatory for their extensive support during the many observing runs of this project. G. J. Hill is especially acknowledged for his commitment at the McDonald Observatory facilities. The authors also thank Claus Gössl for supplying his cosmics filter, Nigel Metcalfe for making number count data available in electronic form, and Klaus Meisenheimer for providing the distortion correction for CAFOS. This research has made use of NASA's Astrophysics Data System (ADS) Abstract Service and the NASA/IPAC Extragalactic Database (NED). The MUNICS project was supported by the Deutsche Forschungsgemeinschaft, *Sonderforschungsbereich 375, Astroteilchenphysik*. CMdO is grateful to the Alexander von Humboldt Foundation for financial support provided during a visit to the Universitäts-Sternwarte München from Sep. 1997 to Aug. 1998.

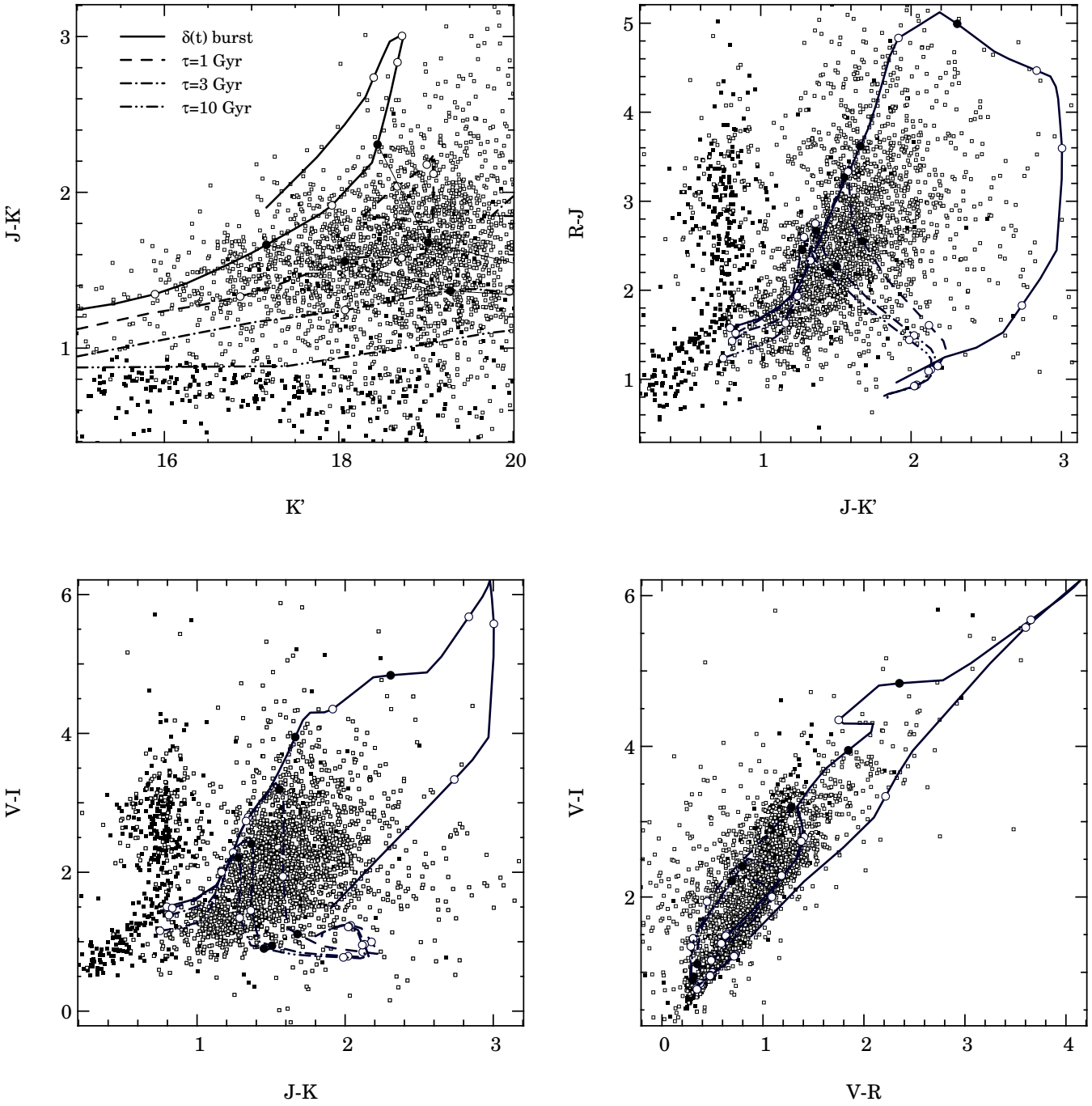

Figure 10. Colour–magnitude and colour–colour diagrammes for MUNICS objects taken from 3 mosaic fields (S2 f1–f4, S6 f5–f8, and S7 f5–f8) containing 2977 sources. Objects classified as stellar are marked with filled squares, extended objects are marked with open squares. Also shown are stellar population synthesis models for different star-formation histories. The model parameters are the same as in Fig. 1. Redshift along the model tracks is marked by circles at a z spacing of 0.5, with $z = 1$ and $z = 2$ being accentuated by filled circles. The lines of constant redshift at $z = 1$ and $z = 2$ are drawn as thin solid lines.